Studying Phase Behavior of Oil/Natural-Gas Systems for Designing Gas-Injection Operations: A Montney Case Study

Son Tran, Sara Eghbali, and **Hassan Dehghanpour,** University of Alberta

Summary

Advances in horizontal drilling and multistage hydraulic fracturing have unlocked tight-oil resources, such as the Montney Formation in the Western Canadian Sedimentary Basin. However, the average oil-recovery factor after primary production is 5 to 10% of the original oil in place. The aims of this study are to investigate phase behavior and to estimate the minimum miscibility pressure (MMP) of the Montney oil/natural-gas systems.

First, we measure the MMPs of the oil/gas systems using the vanishing interfacial tension (VIT) technique. The gas samples are methane (C_1) and mixtures of methane and ethane (C_1/C_2). Second, we perform constant-composition-expansion (CCE) tests to study the phase behavior of the oil/gas systems using a pressure/volume/temperature (PVT) cell. To complement the VIT and CCE tests, we perform bulk-phase tests to visualize vaporizing/condensing phenomena at the oil/gas interface using a visualization cell. Finally, we use the measured CCE and MMP data to calibrate the Peng-Robinson (Robinson and Peng 1978) equation of state (PR-EOS) and predict the MMP of the oil/gas systems using ternary diagrams. The results suggest that the dominant mechanism for developing miscibility conditions for oil/C_1 and oil/C_1/C_2 systems is vaporizing and condensing gas drive, respectively. According to the results of the VIT and CCE tests, increasing C_2 mole fraction in the gas mixtures significantly reduces MMP of the oil/gas system (from 4,366 psi for oil/C_1 to 1,467 psi for oil/C_1/C_2 with 71.3 mol% C_2) and increases the oil-swelling factor (from 1.47 to 1.61 by increasing C_2 mol% from 0 to 70 mol%). The results of visualization tests show that the presence of C_2 in the injection gas significantly enhances oil swelling compared with the pure-C_1 case. We observe vaporizing flows of oil components in all tests and strong condensing flows of C_1 and C_2 into the oil phase in the C_1/C_2 test with increasing gas-injection pressure. The MMP values predicted by plotting two-phase equilibrium data on ternary diagrams appear to be in good agreement with the measured ones. The results can be used to optimize the injection-gas composition and operating pressure in the Montney.

Introduction

Advances in multistage hydraulic fracturing and horizontal drilling have led to the successful development of unconventional oil and gas resources. Low oil-recovery factors after primary production (typically less than 10%) and rapid decline rates are key challenges in developing tight oil formations (Hughes 2013; King 2014; Gherabati et al. 2017). Indeed, these challenges open up opportunities for enhanced-oil-recovery (EOR) operations. With the recent boom of oil production from tight-oil reservoirs, there has been a growing interest in using associated gases for EOR and reducing gas flaring (Jin et al. 2017). Gas injection, in general, has a wide range of objectives, such as pressure maintenance, oil-viscosity reduction, oil swelling, and vaporizing of oil components (Zick 1986).

In a gas huff 'n' puff process, achieving miscibility conditions is important to improve oil recovery. The miscibility conditions can be achieved by either first contact or by multiple contacts (Pedersen et al. 2015). The first-contact miscibility occurs when oil and gas immediately form a single phase at any mixing proportions and at the given pressure and temperature. Multicontact miscibility requires multiple contacts and mass transfer between the oil and injected gas. If the porous medium is represented as a series of mixing cells, the multicontact miscibility can be categorized into two processes: a vaporizing gas drive and a condensing gas drive (Orr 2007). In a vaporizing gas drive, miscibility is achieved by the vaporization of intermediate-oil components into the gas phase. In a condensing gas drive, miscibility is achieved by condensation of gas components into the oil phase.

The MMP of an oil/gas system can be determined by three methods: experimental, numerical modeling, and analytical techniques (Egwuenu et al. 2004). The experimental methods include slimtube, rising-bubble, and VIT tests. MMP can be numerically modeled by the multiple-mixing-cell method (Zick 1986; Ahmadi and Johns 2011). This analytical technique has been developed using key-tie-line identification to speed up the calculation of MMP during oil displacement by a multicomponent gas (Wang and Orr 1997; Jessen et al. 1998).

Slimtube experiments are still an industry standard for MMP estimation because they are able to describe the complex phase behavior and rock/fluid interactions (Yellig and Metcalfe 1980). However, the experiments are slow, and the level of physical dispersion is significantly less than that under field conditions (Johns et al. 2002). Alternatively, VIT and rising-bubble tests have become popular because they are fast and cost effective. In the VIT test, the gas/oil interfacial tension (IFT) is measured at reservoir temperature and at increasing gas-injection pressures. The gas/oil IFTs and capillary heights measured by the pendant-drop-shape analysis (Rao 1997) and the capillary-rise method (Hawthorne et al. 2016) in the VIT technique correspond to first-contact and multiple-contact miscibility, respectively.

Jessen and Orr (2008) argued that experimental MMP methods, such as the VIT and rising-bubble experiments, are suspect because they might not describe the complex phase behavior and displacement processes under reservoir conditions. Therefore, computational methods using tuned EOS for MMP prediction have been developed to mitigate the drawbacks of these experimental methods (Ahmadi and Johns 2011). Ayirala and Rao (2011) demonstrated that the change of the gas/oil ratio in the VIT technique has a negligible effect on the capillary heights and gas/oil IFTs measured at gas/oil equilibrium conditions. Therefore, they concluded that MMP values measured by the VIT technique are independent of the compositional path. Ashrafizadeh and Ghasrodashti (2011) used a mechanistic

parachor model to match the measured MMPs of five gas/oil systems by the VIT technique. Their measured values are within 5% accuracy compared with the MMP values measured by slimtube experiments. On the basis of experimental and modeling studies on Bakken and Permian oil samples, Adekunle and Hoffman (2014), Li and Luo (2017), and Liu et al. (2018) reported that carbon dioxide (CO_2) achieves miscibility with the Bakken oil at lower pressures compared with other hydrocarbon gases. Furthermore, live-oil samples containing solution gas achieve a lower MMP compared with dead-oil samples (Adekunle and Hoffman 2014). Yassin et al. (2018) conducted a bulk-phase visualization study of CO_2/oil systems to understand the gas/oil interactions at the interface. They observed strong vaporizing and condensing flows of oil components and supercritical CO_2 at the gas/oil interface during the pressure-buildup process.

Recently, field tests of dry- and associated-gas EOR have been implemented with promising results in the Eagle Ford Shale (Hoffman 2018; Orozco et al. 2020). The enrichment of injected gas, for example by adding C_2, improves the miscibility between oil and gas. Compared with C_1, C_2 has a higher solubility in oil, lower MMP (Metcalfe 1982), and is usually available at a less-expensive price than propane and butane (McGuire et al. 2017).

The roles of diffusion and advection in transport during the huff 'n' puff process in tight rocks have recently been the subject of considerable debate. Cronin et al. (2019) suggested that the conventional multicontact miscible concepts in a gas huff 'n' puff process are based on advection-dominated transport within the matrix and the absence of large capillary pressures affecting phase-behavior calculations. In addition, they presumed that transport during the soaking period in tight reservoirs might be a completely diffusion-dominated process, and thus, only first-contact miscibility is relevant. Other researchers reported that the diffusion process is the dominant transport mechanism in the matrix of shale-gas and shale-oil reservoirs with permeability less than 10 nd (Olorode et al. 2017) and 1 md (Yu et al. 2015; Lashgari et al. 2019), respectively. Teklu et al. (2014) studied the effects of confined pores on the MMP of CO_2 and a mixture of CO_2 and C_1 with Bakken oil. They noted that the reduction in MMP caused by confinement becomes pronounced when the pore radius is less than 20 nm and is attributed to the critical-temperature and critical-pressure shifts. Moreover, high capillary pressures affect equilibrium liquid/vapor-phase compositions, decreasing the MMP of CO_2 with Bakken oil (Nojabaei et al. 2013; Zhang et al. 2017, 2018).

Measuring multicontact MMP is one of the infrequent phase-behavior experiments in contrast to the CCE test. Therefore, EOS models must be tuned against both CCE and MMP data to accurately predict MMP of the gas/oil systems. The objectives of this study are to investigate phase behavior of the Montney oil and injected-gas systems and determine the ranges of MMP corresponding to different levels of gas enrichment that can be used for field practices, and visually investigate oil swelling and vaporizing/condensing mechanisms at the gas/oil interface during the gas-injection process. We compare the phase behavior and MMPs of oil/C_1 and oil/C_1/C_2 systems using experimental and modeling approaches. We first measure the MMPs of the oil/gas systems using the capillary-rise VIT technique. Second, we perform CCE tests to study the phase behavior of the systems using a PVT cell. Third, we perform bulk-phase tests to visualize oil swelling and vaporizing/condensing flows at the gas/oil interface using a visualization cell. Finally, we use the measured CCE and MMP data to calibrate the PR-EOS and estimate MMPs of the systems using ternary diagrams. To verify the performance of the calibrated EOS models with different numbers of pseudocomponents (PCs), we compare the resulting phase envelopes and check the trend of equilibrium K-values vs. the molecular weights (MWs) of oil components.

Materials

We used a dead-oil sample from a well drilled in the Montney Formation in northwestern Alberta, Canada, and conducted the experiments at representative reservoir pressure (P_{set}) and temperature (T_{set}) of 2,000 psi and 50°C, respectively. The C_1 and C_2 samples used in this study have a purity of 99.999%. The fluid properties and oil compositional analysis are presented in **Table 1** and **Fig. 1,** respectively.

Fluids	Density (kg/m^3)	Viscosity (cp)	Surface Tension (mN/m)
Oil	818.50	2.82	23.95
C_1	0.59	0.01	–
C_2	1.13	0.01	–

Table 1—Physical properties of the Montney dead oil and C_1/C_2 (NIST 2018) at T_{set} and atmospheric pressure.
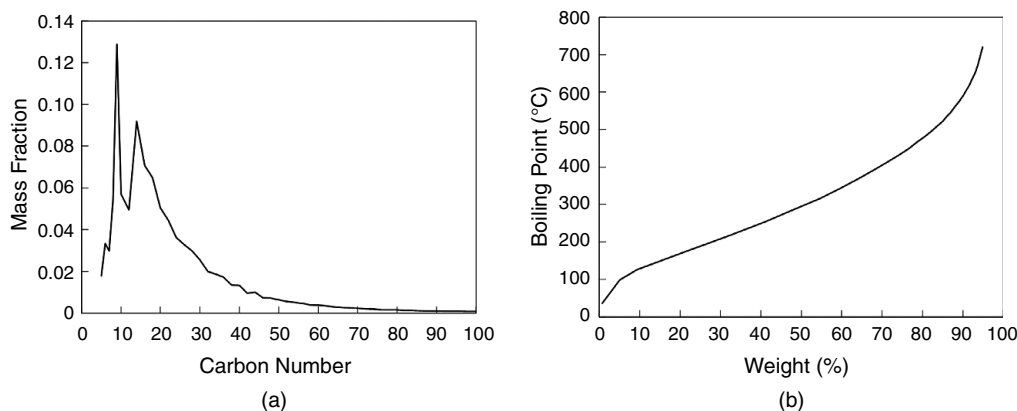

Fig. 1—Simulated distillation results for the Montney oil sample: (a) compositional analysis; (b) true-boiling-point distribution.

Methodology

We conducted a systematic laboratory and modeling study to investigate phase behavior of the oil/C_1 and oil/C_1/C_2 systems.

Experiments. *MMP Measurement by VIT Technique.* The VIT test consists of measuring IFT between the oil and injected gas at increasing pressures and a given temperature (Hawthorne et al. 2016). **Fig. 2** shows a schematic of the visualization system and an image of the capillary tubes and a custom-built gas mixer used for conducting the VIT tests. A detailed technical specification of the visualization system can be found elsewhere (Yassin et al. 2018).
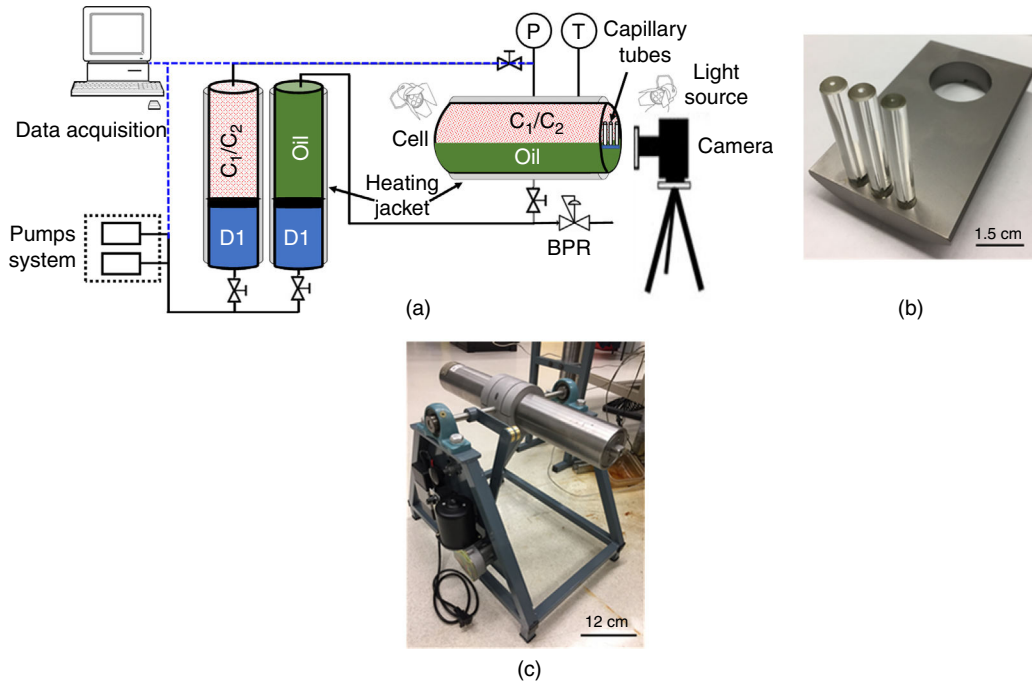

Fig. 2—Experimental setup for conducting VIT tests: (a) the visualization system; (b) three capillary tubes; and (c) a custom-built gas mixer.

The procedure starts with placing three capillary tubes (inner diameters of 0.5, 0.85, and 1.05 mm) in the cell, and injecting gas into the cell at predefined pressure (P) steps. We check the system's leakage by purging the cell/lines several times with the tested gas. The temperature (T) of the cell and accumulators (with oil and gas) are set at T_{set}. The heated oil is injected into the cell until the oil level stops rising inside the capillary tubes. After waiting for approximately 3 minutes for the fluids to equilibrate, we capture images and measure the height of the oil/gas meniscus in each capillary tube from the top of the bulk-oil phase outside the tube. Finally, we plot the height values for the three capillary tubes vs. P and determine P corresponding to zero capillary heights by linear extrapolation. We interpreted this P as the MMP of the three oil/C_1/C_2 systems (with C_1 of 100, 70.1, and 28.7 mol%). We used three capillary tubes to have sufficient data points for extrapolating the trend lines to zero capillary heights.

Mixtures of C_1/C_2 are prepared using two accumulators ($500\,cm^3$ each) and a custom-built gas mixer (Fig. 2c). First, specified amounts of C_1 and C_2 are transferred to two accumulators at room temperature ($T = 21°C$). The mole fractions of C_1 and C_2 (all in the gas state) are calculated according to the accumulator volume ($500\,cm^3$), calculated P, and corresponding compressibility factors to achieve the desired mole ratio (C_1/C_2 ratio of 70:30) at 21°C. The C_1 and C_2 properties are obtained using the NIST chemical webbook (NIST 2018). Second, C_1 and C_2 in the two accumulators are squeezed into the gas mixer that rotates at a speed of 6 rev/min and with an angle of 150° to mix C_1/C_2 mixtures at 21°C for 24 hours. Finally, the gas mixtures are then transferred to a heated accumulator (50°C) and left to equilibrate for 6 hours before starting the VIT tests.

CCE Tests. The CCE tests are performed at reservoir conditions using a PVT cell to measure saturation pressure (P_{sat}) and saturated oil density (ρ_{sat}), and to calculate the swelling factor (SF). **Fig. 3** shows a schematic of the PVT apparatus. The P and T ratings of the PVT cell are 15,000 psig and 199°C, respectively. The temperature of the PVT cell is controlled by an air bath with an accuracy of $\pm0.1°C$. A high-pressure pump controls the pressure of the PVT cell by hydraulic oil. A floating piston is inside the cell and isolates the test fluids from hydraulic oil. The total internal volume of the cell is $112\,cm^3$, with a dead volume of $1.754\,cm^3$. A pressure gauge is used to monitor the cell pressure with accuracy of ±10.5 psig. A cathetometer is in front of the PVT cell to measure the piston height (with an accuracy of $\pm0.016\,cm^3$) for calculating the volume of fluids in the cell.

Table 2 lists the parameters of the CCE tests conducted by following the procedure published in the literature (Whitson and Brulé 2000). We also measure oil density at different P (100 to 4,000 psig) and T (30, 50, and 70°C) values using the PVT cell based on mass balance. Because the mass of the oil in the PVT cell is conserved, the oil density at different experimental conditions can be calculated by

$$\rho_1 = \frac{\rho_{ref} V_{ref}}{V_1}, \quad\dots\dots\dots\dots\dots\dots\dots\dots\dots\dots\dots\dots\dots\dots\dots\dots\dots\dots\dots\dots\dots\dots\dots\dots \text{(1)}$$

where ρ_1 and V_1 are density and volume, respectively, of the oil at given P and T, and ρ_{ref} and V_{ref} are the density and volume, respectively, of the oil at atmospheric pressure (P_{atm}) and the given T. We measure ρ_{ref} and V_{ref} using a densitometer and the PVT cell at P_{atm} and different T values (30, 50, and 70°C). The accuracy of the densitometer is $\pm0.01\,kg/m^3$.

SF is defined as the total volume of oil and dissolved gas at P_{sat} and T divided by the volume of the dead oil (without gas) at the same T and P_{atm},

$$SF = \frac{(V_m)_{P_{sat},T}}{(V_o)_{P_{atm},T}} \times \frac{1}{1-x}, \quad \dots\dots\dots\dots\dots\dots\dots\dots\dots\dots\dots\dots\dots\dots\dots\dots\dots\dots \quad (2)$$

where V_m is the molar volume of the mixture at P_{sat} and T_{set}, V_o is the molar volume of the oil at P_{atm} and T_{set}, and x is the mole fraction of the gas in the mixture.
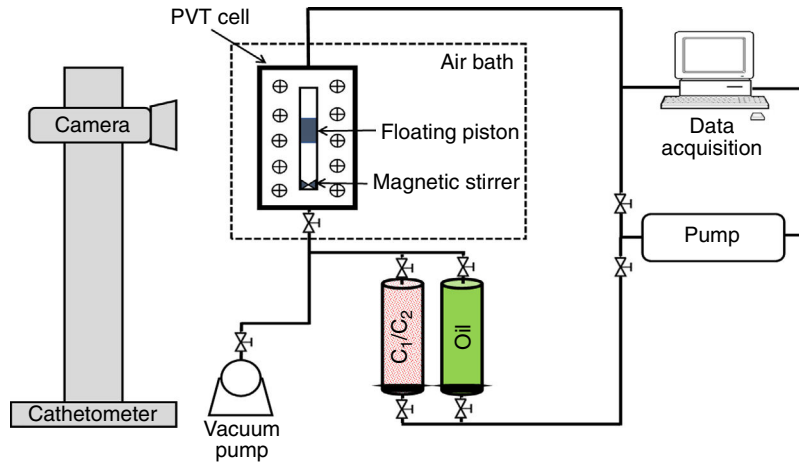

Fig. 3—Schematic of the PVT apparatus for conducting CCE tests.

Feed	Oil/Gas (mol%)	Gas (mol%)	Mass of Oil and Gas (g)		
			Oil	C_1	C_2
1	89.7/10.3	C_1	27.8	0.2	–
2	70.5/29.5	C_1	14.45	0.38	–
3	50.6/49.4	C_1	16.86	1.05	–
4	29.9/70.1	C_1	10.15	1.50	–
5	30.2/69.8	C_2	9.73	–	2.67
6	28.8/71.2	C_1/C_2: 30.0/70.0	21.7	1.02	4.47
7	29.0/71.0	C_1/C_2: 49.6/50.4	31.8	2.46	4.66
8	28.0/72.0	C_1/C_2: 69.7/30.3	35.6	4.06	3.30

Table 2—Experimental conditions of the CCE tests using the PVT cell. The temperature is kept at 50°C in all tests.

Bulk-Phase Visualization Tests. Two visualization tests are conducted for oil/C_1 and oil/C_1/C_2 systems at P_{set} and T_{set} using a visualization cell as shown in Fig. 2a. Before the tests, the cell and connecting lines are cleaned and vacuumed and then checked for leakage by pressurizing the cell with tested gas at 300 psig and monitoring the cell pressure for 4 hours. We conduct two tests (Test 1 for oil/C_1 and Test 2 for oil/C_1/C_2 with 30 mol% of C_2) in the following three steps:
1. Initial conditions: Approximately $255\,cm^3$ of oil is introduced into the cell through the bottom valve at P_{atm} and T_{set}.
2. Pressure buildup: The tested gas is injected into the cell from an inlet valve at the top of the cell to reach P_{set}. Images of the oil/gas interface are captured to observe oil/gas interactions during gas injection. The gas-injection valve is closed at P_{set} to start a soaking period.
3. Pressure decline: During the soaking period, the pressure in the cell will decline as a result of gas dissolution into the oil. The soaking period completes when the pressure in the cell reaches the equilibrium pressure (P_{eq}).

The volume of oil in the cell at initial conditions, end of pressure buildup, and pressure-decline periods are determined by using a spreadsheet-based image-analysis technique. It should be noted that the cell is not equipped with a magnetic stirrer and a floating piston to mix oil and injected gas and to reduce the time to reach equilibrium conditions. Therefore, the equilibrium state is achieved by slow interactions between oil and injected gas. Therefore, the term "oil-swelling factor" is not applicable for this experimental condition. Instead, we define the volume-expansion factor (VEF) of the oil caused by dissolution of the injected gas,

$$VEF = \frac{(V_o)_{P,T_{set}}}{(V_i)_{P_{atm},T_{set}}}, \quad \dots\dots\dots\dots\dots\dots\dots\dots\dots\dots\dots\dots\dots\dots\dots\dots\dots\dots\dots\dots\dots\dots\dots \quad (3)$$

where V_o is the oil volume at an elevated pressure P and T_{set} divided by the initial oil volume (V_i) at P_{atm} and T_{set}. The VEFs at the end of the pressure-buildup and soaking periods are referred to as initial VEF (VEF$_{ini}$) and equilibrium VEF (VEF$_{eq}$), respectively.

EOS Calibration and MMP Prediction. For a gas-injection process, a PR-EOS model needs to be calibrated against the measured CCE and MMP data before being used to predict the MMP of different oil/gas systems (Alavian and Whitson 2010). The main steps to manually calibrate an EOS model include oil characterization, EOS regression, and thermodynamic consistency checks. We plot two-phase equilibrium data from the calibrated EOS models on ternary diagrams to predict the MMPs of the oil/gas systems.

Oil Characterization. The simulated distillation data show that crude oil contains more than 100 different components. It is difficult to measure the thermophysical properties [i.e., critical temperature (T_c), critical pressure (P_c), and acentric factor (ω)] and other EOS parameters for components heavier than C_{20} (Whitson and Brulé 2000). The procedure to split plus fractions, lump oil components into PCs, and estimate critical properties of the PCs can be found elsewhere (Pedersen et al. 1985; Eghbali and Dehghanpour 2018). The oil components are grouped into equal-mass groups with mass-weighted averaging of the properties. Following this method, a four-PC EOS model is recommended by grouping C_1 through C_{10} into PC_1, C_{11} through C_{16} into PC_2, C_{17} through C_{27} into PC_3, and C_{28} through C_{30+} into PC_4. The gas components (i.e., C_1 and C_2) are left ungrouped. To predict the MMP of the oil/gas systems using a ternary diagram, we also group the oil components into one and two PCs. The simplified one- and two-PC EOS models serve as a tool for visualizing and investigating the compositional path on pseudoternary diagrams for oil/C_1 and oil/C_1/C_2 systems.

EOS Regression. The PR-EOS parameters are tuned to match CCE and MMP results for different oil/gas mixtures using the PVTsim software (Calsep A/S 2018). It is essential to obtain a single set of parameters [binary-interaction parameters (BIPs), critical properties, and volume-shift parameters] that can predict the CCE and MMP data of all gas/oil mixtures (in oil/C_1 and oil/C_1/C_2 systems) with acceptable accuracies. The key strategy is using the minimum regression variables (e.g., the BIPs and critical properties of the heaviest PCs) that ensure an optimal solution. The regression variables are adjusted within their estimated uncertainties [i.e., up to 20% of the initially estimated values (Pedersen et al. 2015)]. The following regression variables are used to tune the EOS model:

- BIP. BIPs between C_1/C_2 and the heaviest PCs are tuned to match P_{sat}. The initial values of BIPs between C_1/C_2 and PCs are calculated using the equations available in the literature (Katz and Firoozabadi 1978; Gao et al. 1992).
- Critical properties of PC_3 and PC_4. If tuning BIPs is insufficient to match P_{sat}, T_c and P_c of the heaviest PCs can be tuned accordingly.
- Volume-shift parameters (C_{PEN}). After matching P_{sat}, ρ_{sat} at T_{set} needs to be matched. The C_{PEN} parameters of C_1, C_2, and PCs, using the PVTsim software (Calsep A/S 2018), are adjusted to match ρ_{sat}. The initial values of C_{PEN} are calculated using the equations from Péneloux et al. (1982).

After matching P_{sat} by tuning the BIPs and critical properties of the heaviest PCs, we use the slimtube simulation module in PVTsim (Calsep A/S 2018) to calculate the MMP of the gas/oil system. This iterative process is performed until we reach an acceptable accuracy between P_{sat} and the MMP predictions using the EOS and the measured data.

Thermodynamic Consistency Checks. Because the EOS models are calibrated by changing several regression variables, it is necessary to perform a consistency check to ensure the thermodynamic validity of equilibrium vapor/liquid data and MMP predictions (Whitson and Brulé 2000; Martinsen et al. 2010). Furthermore, using fewer PCs in EOS models can make two-phase equilibrium calculations more efficient, but this might introduce erroneous predictions of phase behavior because of the reduced dimensionality in composition space (Kaul 1999; Kumar 2016). We perform consistency checks for four-, two-, and one-PC EOS models by comparing phase envelopes and plotting equilibrium K-values at different oil/gas compositions vs. MWs of PCs.

MMP Prediction Using Pseudoternary Diagram. Ternary diagrams are useful tools to visualize the phase behavior of a three-component system in a 2D graph (Lake 1989). We perform two-phase equilibrium calculations at pressures of 1,467 to 4,366 psi and T_{set} by using the calibrated EOS models (i.e., two- and one-PC models) and plot the two-phase equilibrium data on pseudoternary diagrams to determine MMPs of the oil/gas systems. Each tie line stands for a set of equilibrated liquid (L) and vapor (V) composition. The L/V region is formed by connecting the locus of L and V compositions of each tie line. **Fig. 4** illustrates the displacement process of a vaporizing gas drive and a condensing gas drive. Fig. 4a presents the oil/C_1-displacement process under a vaporizing gas drive. The vapor phase is enriched with intermediate-hydrocarbon components vaporized from the oil phase (comparing the composition of V_5 with V_1). The process of enriching the vapor phase continues until reaching a critical point at the L/V boundary region. At this point, the vapor phase becomes miscible with the oil phase after several contacts and the length of the equilibrium tie line at miscibility conditions becomes zero (i.e., critical tie line). The oil/C_1/C_2-displacement process under a condensing gas drive is shown in Fig. 4b. Unlike the vaporizing gas drive, where the vapor phase is enriched by intermediate-oil components, a condensing gas drive relies on the condensation of intermediate-oil components from the gas to the oil. The vapor phase becomes richer because oil components transfer more into the gas phase (comparing the composition of V_5 with V_1). In addition, C_2 vaporizes into the gas phase gradually. Furthermore, the liquid phase becomes lighter by condensation of C_2 (comparing the composition of L_5 and L_1).
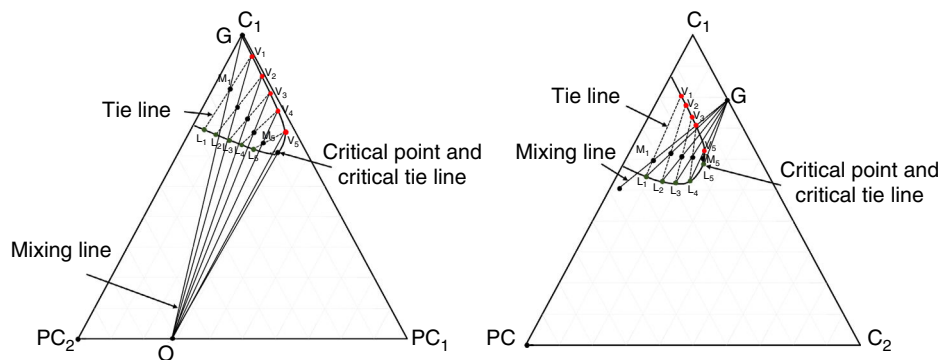

Fig. 4—Pseudoternary diagrams illustrate (a) a vaporizing gas drive and (b) a condensing gas drive. O, G, and M represent oil, gas (C_1 or C_1/C_2 mixture), and oil/gas mixture, respectively.

Results and Discussion

This section reports the results of MMP measurements, CCE and bulk-phase visualization tests, EOS model calibration, and MMP prediction for the oil/C_1 and oil/C_1/C_2 systems.

Measured MMPs of Oil/C_1 and Oil/C_1/C_2 Systems. We conduct the VIT tests to measure the level of capillary rise at increasing gas pressures and T_{set}. Consequently, the MMP is determined from the measured capillary heights. **Fig. 5** shows the measured capillary

heights for capillary tubes with small, medium, and large diameters for three oil/C_1/C_2 systems. The measured MMPs of the three systems with C_1 of 100, 70.3, and 28.7 mol% are 4,350, 2,726, and 1,452 psig, respectively. Fig. 5a includes two images captured at 517 and 1,591 psig that show the reduction of capillary heights with increasing gas pressures. The plot of each capillary tube contains 10 to 16 data points that are adequate to generate reliable trend lines and extrapolate it to the pressures corresponding to zero capillary heights.
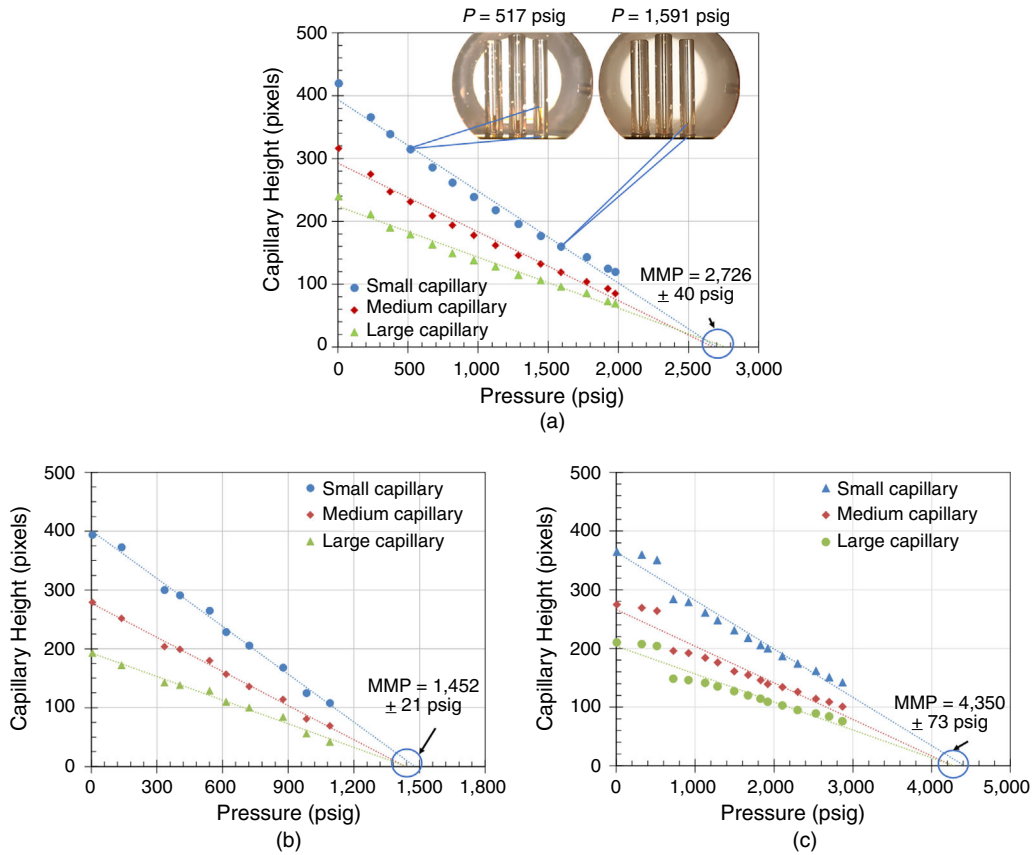

Fig. 5—The results of VIT tests for estimating the MMPs of three oil/C_1/C_2 systems at 50°C: (a) C_1/C_2 = 70.3/29.7 mol%; (b) C_1/C_2 = 28.7/71.3 mol%; (c) C_1/C_2 = 100/0 mol%.

According to Figs. 5b and 5c, MMP of the oil/gas mixtures decrease from 4,350 to 1,452 psig by increasing C_2 from 0 to 71.3 mol%. Metcalfe (1982) reported that the higher concentration of C_1 and C_2 in the rich gas increases and decreases MMPs of oil/gas systems, respectively. In this study, the capillary heights are measured at nearly equilibrium gas/oil conditions at each pressure step. The resulting MMPs satisfy the multicontact-miscibility requirements as reported by Ayirala and Rao (2011) and Hawthorne et al. (2016). Moreover, these measured MMPs will be validated by predicted MMPs using two-phase equilibrium data from the tuned EOS and ternary diagrams in the later sections.

CCE Tests. *Oil/C_1 CCE Test.* Here, we report the results of CCE tests on four oil/C_1 mixtures at T_{set} (see Table 2 for detailed feed compositions). P/V data from the CCE tests on the oil/C_1 systems are shown in **Fig. 6a.** The pressure at which we observe a significant reduction in the slope of the P/V curve is interpreted as P_{sat}. P_{sat} and SF (calculated using Eq. 2) of the oil/gas mixtures at different C_1 mole fractions are plotted in Fig. 6b. The results show that P_{sat} increases with increasing C_1 concentration. For example, P_{sat} increases by more than one order of magnitude when the C_1 concentration increases from 10.3 to 70.1 mol%. The rate of increase in P_{sat} is faster when the C_1 concentration is greater than 50 mol%. We failed to measure P_{sat} at C_1 concentration of 80 mol% because the system pressure gets close to the physical limit of the PVT cell. The SF increases from 1.07 to 1.47 when the C_1 concentration increases from 10.3 to 70.1 mol%.

Oil/C_1/C_2 CCE Test. Here, we report the results of CCE tests on four oil/C_1/C_2 mixtures (see Table 2 for detailed feed compositions). P/V data from CCE tests on the oil/C_1/C_2 systems are shown in Fig. 6c. P_{sat} and SF of the oil at different C_2 mole fractions are plotted in Fig. 6d. P_{sat} increases with decreasing concentration of C_2. For example, P_{sat} in Fig. 6d increases by more than threefold (i.e., from 545 to 1,933 psig) when C_2 concentration decreases from 100 to 30.3 mol%. However, SF exhibits a reverse trend with decreasing C_2 concentration. For instance, SF reduces from 1.76 to 1.49 when C_2 concentration decreases from 70 to 30.3 mol% at T_{set}. SF is the maximum (1.76) for the oil/C_2 system. It should be noted that C_2 is more soluble in oil compared with C_1 at the same P and T.

Calculated Oil Density at Different P and T. We correlate the calculated density from the oil-volume measurements using the PVT cell at different P and T using the Tait equation (Dymond and Malhotra 1988). The measured oil densities at different P and T_{set} are used to determine ρ in the CCE tests:

$$\rho(T,P) = \frac{\rho_{ref}(T,P_{atm})}{1 - \beta \ln \left(\frac{B + 0.0069P}{B + 0.1} \right)}, \quad \dots \dots \dots \dots \dots \dots \dots \dots \dots \dots \dots \dots \dots \dots \dots \dots \dots \dots \dots \dots (4)$$

$$\rho_{\text{ref}}(T, P_{\text{atm}}) = 765.6168 + 0.8544T - 0.0021T^2, \quad \dots\dots\dots\dots\dots\dots\dots\dots\dots\dots\dots\dots\dots\dots\dots\dots \quad (5)$$

$$\beta = 0.2054 - 5.6598 \times 10^{-4}T, \quad \dots\dots\dots\dots\dots\dots\dots\dots\dots\dots\dots\dots\dots\dots\dots\dots\dots\dots\dots\dots\dots\dots\dots \quad (6)$$

$$B = 118.5120 - 1.6839 \times 10^5 T^{-1} + 4.4508 \times 10^7 T^{-2}, \quad \dots\dots\dots\dots\dots\dots\dots\dots\dots\dots\dots\dots\dots\dots \quad (7)$$

where T is temperature (in K), P is pressure (in psig), and ρ is density (in kg/m^3). The parameters in Eq. 5 are determined by fitting the measured ρ_{ref}. We use Eq. 1 to calculate oil density, $\rho(T, P)$. The parameters in Eqs. 6 and 7 are determined by regressing Eq. 4. **Fig. 7** shows the measured and calculated densities using Eqs. 4 through 7. Detailed oil-density data at different P and T can be found in Appendix A.
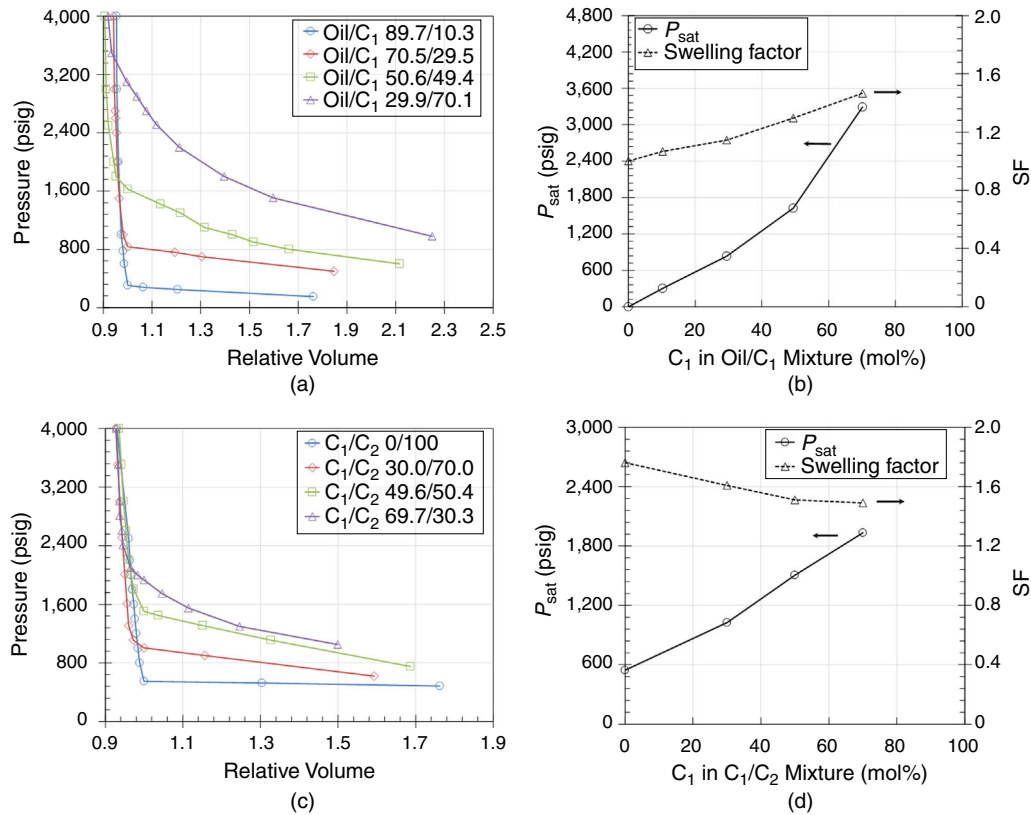

Fig. 6—The results of CCE tests, P_{sat}, and calculated SF at 50°C: (a, b) for oil/C$_1$ systems and (c, d) for oil/C$_1$/C$_2$ systems.
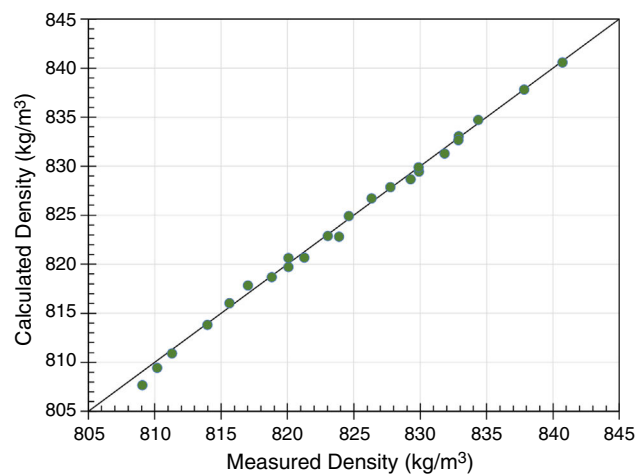

Fig. 7—Comparison of the measured oil density at different pressures and temperatures with calculated density using the Tait equation.

The average absolute relative deviation (AARD) for the calculated oil densities from the experimental data is calculated by

$$AARD = \frac{1}{N} \sum_{j=1}^{N} \left| \frac{\rho_j^{cal} - \rho_j^{exp}}{\rho_j^{exp}} \right|, \quad \dots\dots\dots\dots\dots\dots\dots\dots\dots\dots\dots\dots\dots\dots\dots\dots\dots\dots\dots\dots \quad (8)$$

where ρ_j^{cal} and ρ_j^{exp} are the calculated and measured values, respectively, and N is the number of data points. The AARD for the calculated oil density is 0.035%.

Bulk-Phase Visualization Tests. Fig. 8 shows images of gas/oil interfaces in the cell in two visualization tests. In each test, the captured images correspond to the initial conditions of the test (at P_{atm}, T_{set}) (Fig. 8a), the end of the pressure buildup (at P_{set}, T_{set}) (Fig. 8b), and the equilibrium state (at P_{eq}, T_{set}) (Fig. 8c). In general, it takes approximately 0.27 to 0.29 hours to pressurize the cell from 0 to P_{set} in the two tests. We observe oil volumes shrinking (VEF_{ini} of 0.94 in Test 1 and 0.98 in Test 2) during the pressure buildup. P_{eq} values of Tests 1 and 2 are 1,654 and 1,551 psig, respectively. Consequently, equilibrium times in Tests 1 and 2 are 67 and 60 hours, respectively. VEF_{eq} values at the end of the soaking period in Tests 1 and 2 are 1.08 and 1.28, respectively.
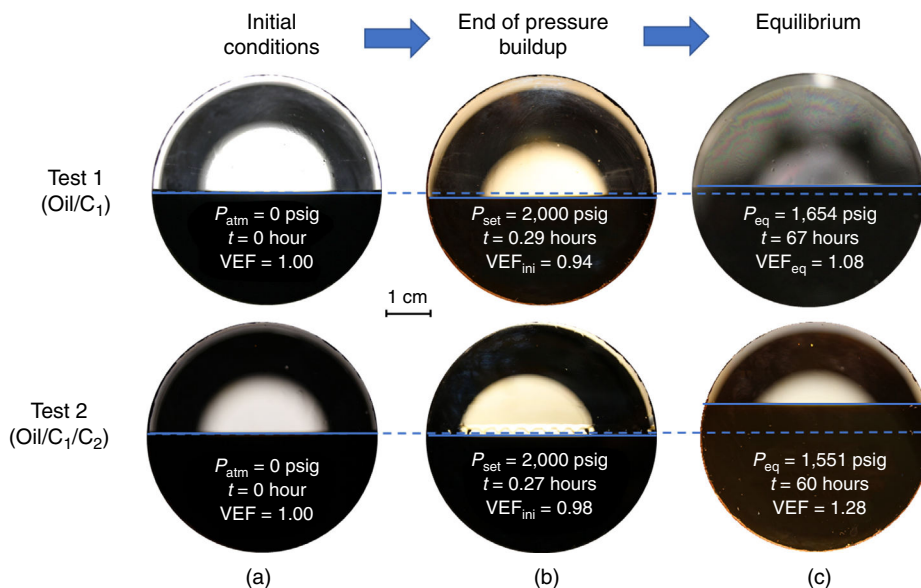

Fig. 8—Images of oil/gas interfaces at (a) initial conditions at P_{atm}, (b) end of pressure buildup at P_{set}, and (c) equilibrium at P_{eq}. The temperature is kept at 50°C during the experiment.

At the equilibrium, Test 2 reaches P_{eq} faster than Test 1, suggesting a higher diffusion rate of C_2 in the oil. By adding 30 mol% C_2, P_{eq} reduces from 1,654 to 1,551 psig, indicating an increase in solubility of the gas phase (i.e., C_1/C_2) compared with the case with pure C_1. The reduction of VEFs at the end of the pressure buildup in both tests indicates that the oil phase is compressed with increasing injection pressure. Because C_2 is more soluble in oil than C_1 at the same P and T, the VEF_{ini} and VEF_{eq} in Test 2 are higher than those of Test 1. This means that the presence of C_2 in the injection gas enhances oil swelling compared with the C_1 case. Moreover, the gas phase in initial conditions (Fig. 8a) is transparent. At the end of the pressure buildup (Fig. 8b), the gas phases in Tests 1 and 2 turn yellowish. This observation suggests that oil components are transferred from the oil phase to the gas phase, and this is more pronounced in Test 2.

Fig. 9 shows the interactions at the oil/gas interfaces during the pressure-buildup process in Tests 1 and 2 at 50°C. The horizontal brown line is the initial level of the oil phase that is compressed downward during the pressure buildup. The upward red arrows in Fig. 9a indicate vaporizing flows of oil components at the oil/C_1 interface. The magnified image of the oil/C_1 interface shows a yellow region on top of the oil phase. The yellow color indicates the presence of oil components transferred from the bulk-oil phase toward the bulk-gas phase, and becomes darker in the region close to the oil/gas interface. This is caused by the upward transport of vaporized oil components within the gas phase over time. We did not observe condensing flows during Test 1.

Fig. 9b shows the vaporizing of oil components and condensing flows of C_1 and C_2 at the oil/C_1/C_2 interface during pressure buildup in Test 2. Figs. 9b(i) through 9b(iii) show the magnified images of the oil/gas interface at three different times. The time frame between Figs. 9b(i) and 9b(iii) is approximately 0.22 hours. At $t = 0.03$ hours [Fig. 9b(i)], condensing flows (downward green arrows) of C_1 and C_2 occur and traces of vaporized oil components (yellow spots) are observed in the gas phase. We notice a layer on top of the oil phase (in a blue dotted rectangle) that might be a mixture of C_1/C_2 and vaporized oil components. Under these conditions (pressure and temperature of 740 psig and 50°C, respectively), C_1 and C_2 are in supercritical states with corresponding densities of 32.41 and 94.73 kg/m³ (NIST 2018), respectively. The gas phase becomes yellowish because of the stronger vaporizing flows at $t = 0.08$ hours [Fig. 9b(ii)]. This bright-yellow region has a color gradient similar to what we observed in Test 1 (Fig. 9a) in terms of color and location. Furthermore, this continuous-concentration gradient becomes stronger with increasing pressure, as shown in Fig. 9b(iii). The heavier oil components and C_1/C_2 form a thick and dark-yellow layer on top of the oil phase. This might be attributed to the effects of gravity and mass transport caused by the concentration gradient. When the pressure increases to 1,850 psig at $t = 0.25$ hours, the appearance of several droplets indicates stronger condensing flows of C_1, C_2, and oil components into the oil phase. The vaporizing and condensing flows persist during the soaking process and cease at equilibrium conditions, as shown in Fig. 8c.
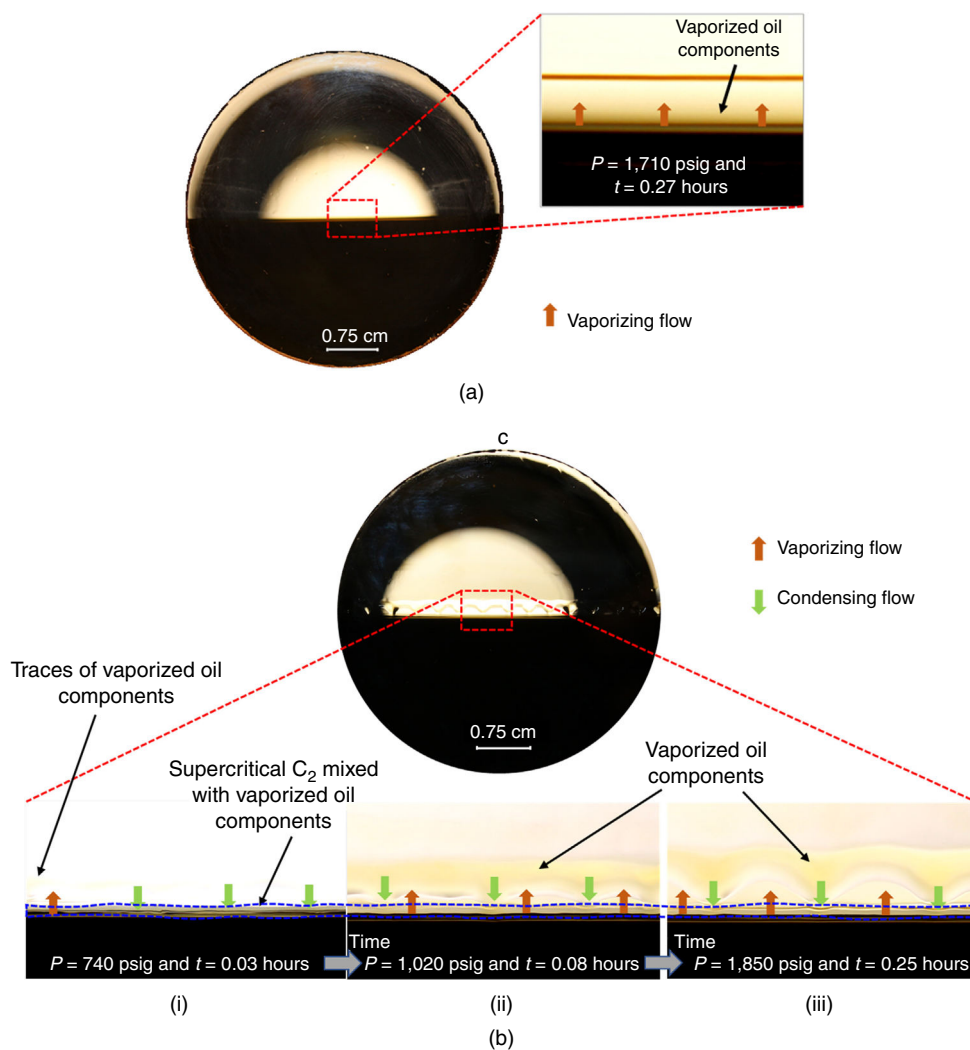
Fig. 9—Images captured at oil/gas interfaces during the pressure-buildup process: (a) vaporizing flows in the oil/C_1 test; (b) vaporizing/condensing flows in the oil/C_1/C_2 test at 50°C.

EOS Calibration and MMP Prediction. P_{sat}, SF, and density data from the CCE tests are used to calibrate one-, two-, and four-PC EOS models and predict the phase behavior/MMP of the oil/gas systems. Regression variables include BIPs between gas/PCs, critical properties of PCs (T_c, P_c), and C_{PEN}. Hydrocarbon/hydrocarbon (HC/HC) BIPs of the PCs are assumed to be zero for the PR-EOS. C_{PEN} parameters are tuned separately to match ρ_{sat}. For consistency, we aim to obtain a single set of parameters for the PR-EOS model that matches the CCE and MMP data of both oil/C_1 and oil/C_1/C_2 systems.

Calibrating EOS Model with Four PCs. *Oil/C_1 System.* **Table 3** summarizes the related regression parameters for a four-PC EOS model that is calibrated against oil/C_1 CCE data. **Table 4** presents the optimized BIP values between C_1 and the PCs. The HC/HC BIPs are set to zero [default values in PVTsim software (Calsep A/S 2018)]. The values of ρ_{sat} were matched by manually regressing the C_{PEN} of PCs and C_1. Because the ρ_{sat} value calculated by EOS is lower than those from CCE tests, we increase the initial C_{PEN} of the PCs and C_1 stepwise and calculate the corresponding ρ_{sat} until we obtain a reasonable match. The regression was performed prudently with due consideration of the physical trend of EOS parameters with MWs of PCs (e.g., BIPs between C_1 and PCs increase monotonically with increasing MWs of PCs).

Component	z_i	MW	P_c (psi)	T_c (°C)	ω	V_c (cm³/mol)	C_{PEN} (cm³/mol)
C_1	0	16.04	667.17	−82.55	0.008	99.00	−1.41
PC_1	46.81	106.12	425.25	296.91	0.374	451.19	49.84
PC_2	29.00	170.91	298.63	404.49	0.595	725.45	102.73
PC_3	16.11	275.57	177.53	473.01	0.777	1126.81	253.90
PC_4	8.08	518.47	96.74	537.81	0.983	1767.59	428.58

Table 3—Properties of components in the four-PC EOS model calibrated against oil/C_1 CCE and MMP data.

	C_1	PC_1	PC_2	PC_3	PC_4
C_1	–	–	–	–	–
PC_1	7.33×10^{-4}	–	–	–	–
PC_2	9.33×10^{-4}	0	–	–	–
PC_3	20×10^{-4}	0	0	–	–
PC_4	35×10^{-4}	0	0	0	–

Table 4—Optimized BIP of the four-PC EOS model calibrated against the oil/C_1 CCE and MMP data.

Table 5 compares P_{sat}, SF, and ρ_{sat} from the CCE tests with the values predicted by the EOS for oil/C_1 systems. The EOS model predicts P_{sat}, SF, and ρ_{sat} of the oil/C_1 systems with AARDs of 8.01, 4.37, and 11.97%, respectively. SF and ρ_{sat} exhibit reverse trends vs. the increasing mole fractions of C_1 in both experimental and predicted data. For instance, the measured SFs increase from 1.07 to 1.47 with increasing C_1 concentration from 10.3 to 70.1%, whereas the measured ρ_{sat} decreases from 804.4 to 766.1 kg/m³. By dissolving more C_1, the volume of oil increases, which leads to higher SF and lower oil density.

C_1 in Oil/C_1 Mixture (mol%)	Experimental Results			Predictions from Four-PC EOS Model		
	P_{sat} (psi)	SF (fraction)	ρ_{sat} (kg/m³)	P_{sat} (psi)	SF (fraction)	ρ_{sat} (kg/m³)
10.3	320	1.07	804.4	259	1.02	959.6
29.5	849	1.14	790.7	844	1.09	899.2
49.4	1,640	1.30	779.5	1,647	1.19	818.3
70.1	3,305	1.47	766.1	2,871	1.47	690.3
AARD (%)				8.01	4.37	11.97

Table 5—Comparison of the measured data and EOS predictions for the oil/C_1 system.

Oil/C_1/C_2 System. **Table 6** summarizes the related regression parameters for the four-PC EOS model that is calibrated against oil/C_1/C_2 CCE data. **Table 7** presents the optimized BIP values between C_1/C_2 and PCs. It should be noted that the parameters in Table 6 are identical to those in the four-PC EOS model of oil/C_1/C_2, except for the BIP (between C_2 and PCs) and C_{PEN} values of C_2.

Component	z_i	MW	P_c (psi)	T_c (°C)	ω	V_c (cm³/mol)	C_{PEN} (cm³/mol)
C_1	0	16.04	667.17	–82.55	0.008	99.00	–1.41
C_2	0	30.07	708.37	32.25	0.098	148.00	–5.99
PC_1	46.81	106.12	425.25	296.91	0.374	451.19	49.84
PC_2	29.00	170.91	298.63	404.49	0.595	725.45	102.73
PC_3	16.11	275.57	177.53	473.01	0.777	1126.81	253.90
PC_4	8.08	518.47	96.74	537.81	0.983	1767.59	428.58

Table 6—Properties of components in the four-PC EOS model calibrated against the oil/C_1/C_2 CCE and MMP data.

	C_1	C_2	PC_1	PC_2	PC_3	PC_4
C_1	–	–	–	–	–	–
C_2	0	–	–	–	–	–
PC_1	7.33×10^{-4}	0	–	–	–	–
PC_2	9.33×10^{-4}	0	0	–	–	–
PC_3	20×10^{-4}	1×10^{-4}	0	0	–	–
PC_4	35×10^{-4}	3×10^{-4}	0	0	0	–

Table 7—Optimized BIP values of the four-PC EOS model calibrated against the oil/C_1/C_2 CCE and MMP data.

Table 8 compares P_{sat}, SF, and ρ_{sat} from the CCE tests with the EOS predictions for the oil/C_1/C_2 systems. The EOS model predicts P_{sat}, SF, and ρ_{sat} of the oil/C_1/C_2 systems with AARDs of 4.75, 3.51, and 10.96%, respectively. The measured SFs decrease from 1.76 to 1.49 with decreasing C_2 concentration from 100 to 30.3%, while the measured ρ_{sat} increases from 732.9 to 764.4 kg/m³.

Calibrating EOS Models with Two and One PCs. We use ternary diagrams to graphically study the mechanisms of developing miscibility conditions in different oil/gas systems. On the ternary diagram, pure components (C_1 and C_2) in the injected gas usually occupy one to two apexes, leaving the remaining apexes for the PCs. Therefore, it is not possible to plot the composition of mixtures consisting of C_1/C_2 and four PCs on the ternary diagram. Here, we purposely introduce EOS models with two and one PCs, allowing us to

illustrate three-component phase behavior on the ternary diagram. Although these two simplified EOS models are well-calibrated against the relevant CCE data, reducing the dimension of compositional space affects the accuracy of the predicted phase behavior. The models' parameters can be found in Appendix B.

C_1/C_2 in Oil/Gas Mixture (mol%)	C_2 in C_1/C_2 Mixture (mol%)	Experimental Results			Predictions from Four-PC EOS Model		
		P_{sat} (psi)	SF (fraction)	ρ_{sat} (kg/m^3)	P_{sat} (psi)	SF (fraction)	ρ_{sat} (kg/m^3)
69.8	100	560	1.76	732.9	544	1.62	662.7
71.2	70.0	1,034	1.61	746.9	1,101	1.58	664.0
71.0	50.4	1,515	1.51	755.4	1,545	1.55	666.8
72.0	30.3	1,945	1.49	764.4	2,093	1.52	677.1
AARD (%)					4.75	3.51	10.96

Table 8—Comparison of the measured data and EOS predictions for the oil/C_1/C_2 system.

Thermodynamic Consistency Checks. Consistency checks using phase envelopes and equilibrium K-values vs. MWs of the PCs are necessary to ensure that the predicted two-phase equilibrium data from calibrated EOS models are thermodynamically reliable. **Fig. 10** shows phase envelopes of one-, two-, and four-PC EOS models. Fig. 10a shows the phase envelopes of oil/C_1 systems (from two- and four-PC models) with oil/C_1 molar fractions of 29.9/70.1 mol%. We compare experimental P_{sat} values with predicted values at T_{set}. The two- and four-PC EOS models predict P_{sat} with AARDs of 6.05 and 13.25%, respectively. Fig. 10b shows the phase envelopes of oil/C_1/C_2 systems (one- and four-PC models) with oil/gas and C_1/C_2 molar fractions of 28.0/72.0 mol% and 69.7/30.3 mol%, respectively. The one- and four-PC EOS models predict P_{sat} with AARDs of 3.03 and 1.69%, respectively. The phase-envelope comparison suggests that predicted P_{sat} values using one-, two-, and four-PC EOS models at T_{set} are reasonable and the two-phase equilibrium calculations using one- and two-PC EOS models can be used for MMP prediction. We encountered technical challenges for matching P_{sat} of the oil/C_1 systems, especially at the gas/oil molar fractions of 70/30 mol%, as reflected in Table 5 and Fig. 10a. The deviation of predicted from measured P_{sat} at this GOR might be caused by the absence of light components in the oil, leading to a higher MMP calculated by slimtube simulation in PVTsim (Calsep A/S 2018). Although the critical points and dewpoint regions of the oil/C_1 and oil/C_1/C_2 systems are clearly outside the operating conditions (isothermal at 50°C), the comparative phase envelopes show a disparity, especially in the case of one vs. four PCs (Fig. 10b).
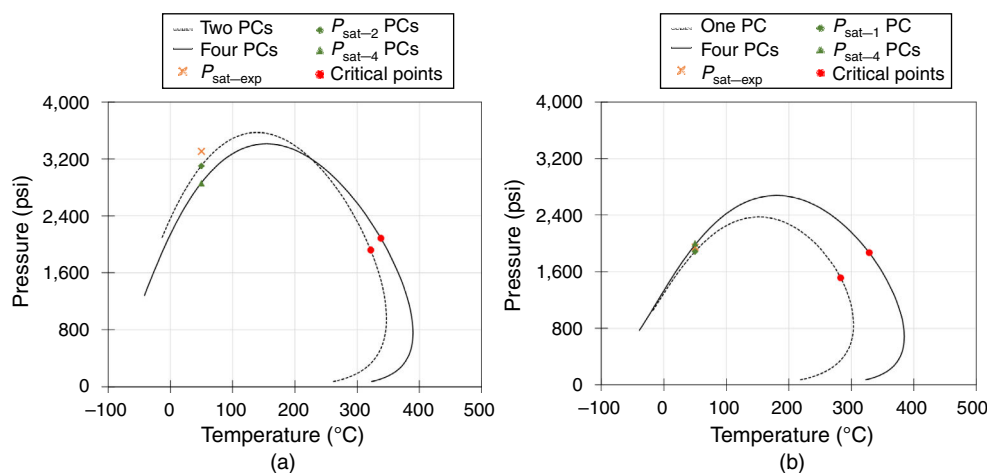

Fig. 10—Comparison of experimental and predicted P_{sat} using phase envelopes at 50°C: (a) two- and four-PC EOS models with C_1 of 70.1 mol%; (b) one- and four-PC EOS models with C_1/C_2 of 69.7/30.3 mol%.

Fig. 11 depicts the trend of K-values vs. MWs for the PCs of the four-PC EOS models at P_{set} and T_{set}. The detailed two-phase equilibrium data for the oil/C_1 (Compositions 1 through 4) and oil/C_1/C_2 (Compositions 5 through 8) systems can be found in Appendix C. K-values in Figs. 11a and 11b monotonically decrease with increasing MW of the PCs. The observed trends suggest that the calibrated EOS models are thermodynamically reliable and can be used for phase-behavior predictions. We also performed consistency checks on the trend of K-values for one- and two-PC EOS models, and the results can be found in Appendix C.

MMP Calculation Using Pseudoternary Diagrams. We estimate the MMP values of the oil/C_1/C_2 systems using two-phase equilibrium data from the calibrated EOS models and pseudoternary diagrams. For consistency, we also perform MMP predictions using the slimtube simulation module in PVTsim software (Calsep A/S 2018) for the four-PC model. **Table 9** summarizes the measured and predicted MMPs for the oil/C_1/C_2 systems with C_1 of 100, 70.1, and 28.7 mol%. At fixed oil/gas molar fractions and T, increasing C_1 molar fraction increases MMP of the system. For instance, the measured MMP increases approximately threefold (i.e., from 1,467 to 4,366 psi) when C_1 increases from 28.7 to 100 mol% at T_{set}. As mentioned in the Methodology section, the purpose of calibrating the one- and two-PC EOS models is only to visualize and understand the changes in the compositional path (phase envelope) relative to changes in pressure and gas composition on a pseudoternary diagram. Although the predicted MMPs using pseudoternary diagrams (two- and one-PC models) are close to the values predicted by the slimtube simulation (four-PC EOS model) and the experiments, we

believe that the MMP values predicted by four-PC EOS are more reliable. In fact, MW of the heaviest PC reduced by decreasing the numbers of PCs (518 g/mol for four PCs, 222 g/mol for two PCs, and 186 g/mol for one PC) because of the high fractions of light-oil components in the oil. This reduction in MW might facilitate the matching process for MMP and P_{sat} of one and two PCs compared with those of four PCs. According to the results of Kaul (1999) and Whitson (1983), the accuracy of MMP prediction depends on the MW of intermediates and heavy fractions and the spectra of components represented by the PCs.
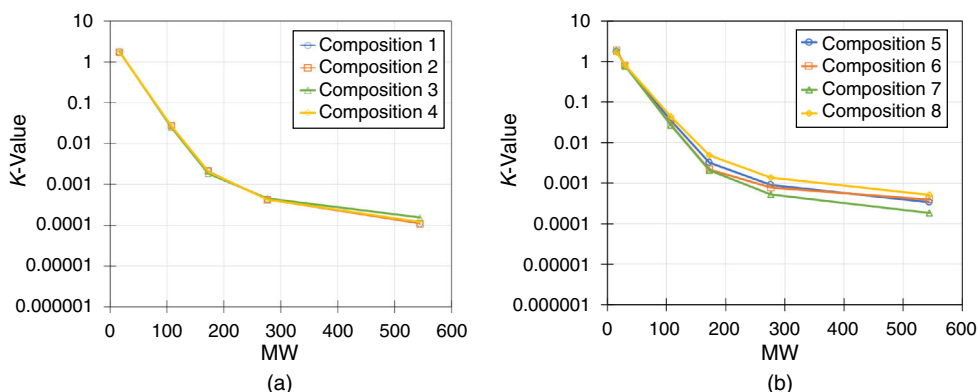

Fig. 11—Equilibrium *K*-values vs. MWs of the components in the four-PC EOS models for (a) oil/C$_1$ system and (b) oil/C$_1$/C$_2$ system at 2,000 psi and 50°C.

C$_1$/C$_2$ (mol%)	Experimental MMP (psi)	MMP Predictions from EOS Models (psi)		
		Four PCs	Two PCs	One PC
C$_1$/C$_2$: 100/0	4,366	4,470	4,460	–
C$_1$/C$_2$: 70.3/29.7	2,741	2,676	–	2,698
C$_1$/C$_2$: 28.7/71.3	1,467	1,437	–	1,480

Table 9—Comparison of the measured and predicted MMPs for the oil/C$_1$ and oil/C$_1$/C$_2$ systems. The slimtube simulation and pseudoternary diagrams are used to calculate MMPs for four-PC and one- and two-PC EOS models, respectively.

Multicontact-Miscibility Achievement by Increasing Gas-Injection Pressure. As demonstrated previously, the key mechanism for developing miscibility conditions for the oil/C$_1$ system is vaporizing gas drive. Increasing injection pressure leads to shrinkage of the two-phase region until reaching MMP of the oil/gas system. **Fig. 12** illustrates pseudoternary diagrams that are built from the two-phase equilibrium data of the two-PC EOS model at 2,000 and 4,460 psi.
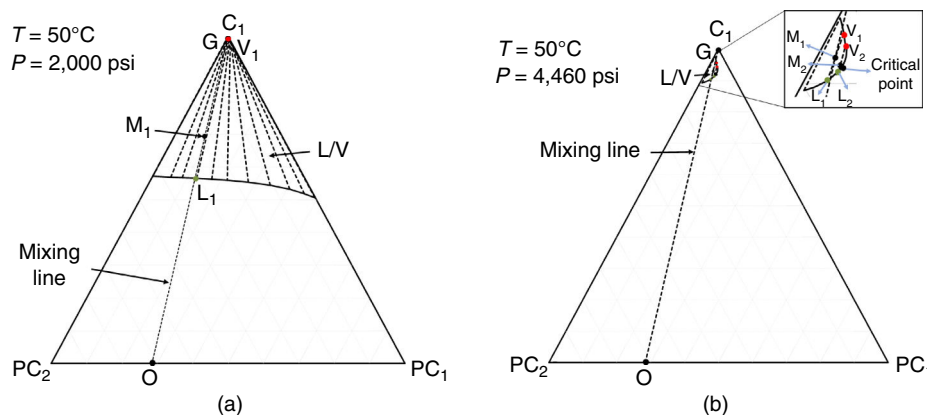

Fig. 12—Pseudoternary diagrams of the oil/C$_1$ system at 50°C and gas-injection pressure of (a) 2,000 psi and (b) 4,460 psi. O and G stand for oil and gas, respectively.

At 2,000 psi, Fig. 12a shows that after the first contact with the oil, the overall mixture composition is on the mixing line within the L/V region. Any further contacts between the enriched-gas phase and oil do not result in shorter mixture tie lines. This is because the enrichment level is inadequate to move the injection-gas composition, V$_1$, further toward the PC$_1$ and PC$_2$. In this case, the oil/gas displacement does not reach miscible conditions. However, by increasing the injection pressure from 2,000 to 4,460 psi (Fig. 12b), which is the MMP of this oil/C$_1$ system, we observe a significant shrinkage of the L/V region. In the L/V region, the gas phase is enriched with intermediate-oil components from the original oil (compare composition of V$_2$ with that of V$_1$). The mixture composition moves along a composition path from M$_1$ toward the boundary of the L/V region and eventually arrives at the critical point (92 mol% C$_1$, 3 mol% PC$_1$, and 5 mol% PC$_2$).

Multicontact-Miscibility Achievement by Changing the Injected-Gas Composition. Under field conditions, increasing the gas-injection pressure is not always feasible because of limitations related to gas compressors. Alternatively, we can change gas composition to arrive at a lower MMP for a given oil/gas system by condensing gas drive, as shown in **Fig. 13.** The gas composition can be changed by varying the C_2 molar fraction along the C_1/C_2 side of the diagram. The dominant mechanism for developing miscibility conditions for the oil/C_1/C_2 system is condensing gas drive. Figs. 13a and 13b illustrate pseudoternary diagrams that are built from two-phase equilibrium data of the one-PC EOS model with C_1/C_2 molar fractions of 70.3/29.7 mol% and 28.7/71.3 mol%. The MMPs of the two systems are 2,698 and 1,480 psi, respectively. The critical point in Fig. 13a has 60.5 mol% C_1, 29.5 mol% C_2, and 10 mol% PC, while it has 28 mol% C_1, 67 mol% C_2, and 5 mol% PC in Fig. 13b.
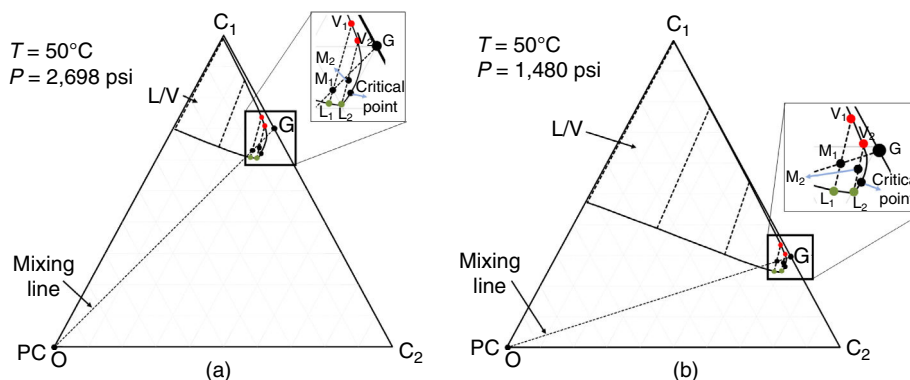

Fig. 13—Pseudoternary diagrams of oil/C_1/C_2 systems at 50°C: (a) C_1/C_2 = 70.3/29.7 mol%; (b) C_1/C_2 = 28.7/71.3 mol%. O and G stand for oil and gas, respectively.

Implications for the Field Huff 'n' Puff Gas-Injection Design. We studied the phase behavior of Montney oil/C_1/C_2 to understand how the injected gas will perform downhole. The visualization results suggest that oil swelling is an important oil-recovery mechanism in the gas-injection huff 'n' puff process. Theoretically, the oil swelling is expected to increase the visualization cell's pressure during the soaking period. However, P_{eq} indicates an opposite trend, suggesting that the diffusion of gas to the oil overcomes the oil-swelling effect.

Miscibility conditions depend on oil composition, injection-gas composition, pressure, and temperature. In oilfield applications, it might be practical to achieve miscible conditions by adjusting the gas-injection pressure and composition at the surface. Knowing the range of MMPs corresponding to different levels of hydrocarbon enrichment helps operators in designing/optimizing the gas-compression system, reservoir-simulation-study sensitivity for the gas-injection EOR scenarios, and a long-term fieldwide development plan with consideration to the source of gas supply and gathering facility. For instance, it is impossible to inject dry gas (C_1 only) at a pressure higher than the MMP (4,366 psi in this case study) because that pressure is well over the gas-compressor capacity and might introduce geomechanical complications from refracturing the formation. Instead, a viable solution is to increase the molar fraction of C_2 in the injected gas to, for instance, 70 mol% to cut the MMP to less than 1,500 psi, which likely meets the existing gas-compression capacity. Finally, by understanding developed miscibility conditions of the Montney oil/C_1/C_2 systems at reservoir conditions, the bottomhole injection pressure can be estimated to optimize the oil recovery in this reservoir.

Limitations

We present the following limitations:
- The oil swelling and MMP of oil/gas systems are susceptible to the presence of light-oil components. The oil SF is expected to be higher by using live oil because light components enhance the solubility of gas in the oil. On the other hand, P_{sat} and MMP values are lower when using live oil. The light components (C_1 through C_4) in the live oil help reduce the MMP of the gas/oil mixtures.
- The accuracy of MMP measured by the VIT technique and the oil swelling in the visualization tests depend on the quality of images captured over the course of the experiments. Because C_2 is in the supercritical state at pressures greater than 707 psia and 50°C, the image quality decreases because of the cloudiness of the injected gas.
- The gas mixtures undergo phase changes (from supercritical to gaseous state) when they are transferred from the heated accumulator at high pressure to the heated visualization cell at vacuum pressure. This affects the diffusion of gas to the oil at the early stages of the VIT and bulk-phase visualization tests.
- Lumping the oil components to PCs in the calibrated EOS affects the accuracy of predicted phase behavior and the MMP of the oil/gas systems.

Conclusions

We characterized the phase behavior of oil/natural-gas systems by conducting CCE tests between an oil sample from the Montney Formation and injection gases (C_1 and mixture of C_1/C_2). MMPs of different oil/gas systems were measured using the capillary-rise VIT technique. To complement the CCE and VIT tests, we performed bulk-phase tests to visualize oil/gas interactions at the interface using a visualization cell. PR-EOS models were regressed to match the data from CCE and VIT tests and predict the MMP values of the oil/gas systems at the reservoir temperature of 50°C using ternary diagrams. We summarize the following key points from the study:
1. The dominant mechanism for developing miscibility conditions is vaporizing gas drive for the oil/C_1 system and condensing gas drive for the oil/C_1/C_2 systems.
2. The VIT tests indicate that increasing the C_2 molar fraction in the gas mixtures significantly decreases the MMP of the oil/gas mixtures (from 4,366 psi for oil/C_1 to 1,467 psi for oil/C_1/C_2 with 71.3 mol% C_2).

3. The presence of C_2 in the injection gas increases the oil swelling factor (i.e., from 1.47 to 1.61) by increasing C_2 molar fraction from 0 to 70 mol%.

4. Vaporizing flow of oil components to the gas phase occurs in all visualization tests. The condensation of C_2 into the oil phase in the C_1/C_2 test leads to a higher oil-volume expansion compared with the pure-C_1 case.

5. Reasonable PR-EOS models were calibrated against CCE and MMP data. Achieving consistent and physical K-values from the two-phase equilibrium calculations using calibrated EOS models suggests that the models are thermodynamically reliable and can be used to predict the MMPs of the oil/gas systems. The predicted MMPs by plotting two-phase equilibrium data on ternary diagrams have good agreement with the measured ones.

6. The miscibility conditions can be achieved by either increasing gas-injection pressure (from a reservoir pressure of 2,000 psi up to approximately 4,366 psi in the oil/C_1 system) or increasing the molar fraction of C_2 in the gas mixtures (from 29.7 to 71.3 mol% to reduce the MMP of oil/gas systems from 2,741 to 1,467 psi).

The findings presented in this study lead to an improved understanding of the phase behavior and processes leading to miscibility conditions that can be applied to design more effective natural-gas huff 'n' puff operations in tight oil formations.

Acknowledgment

References

Adekunle, O. O. and Hoffman, B. T. 2014. Minimum Miscibility Pressure Studies in the Bakken. Paper presented at the SPE Improved Oil Recovery Symposium, Tulsa, Oklahoma, USA, 12–16 April. SPE-169077-MS. https://doi.org/10.2118/169077-MS.

Ahmadi, K. and Johns, R. T. 2011. Multiple-Mixing-Cell Method for MMP Calculations. *SPE J.* **16** (4): 733–742. SPE-116823-PA. https://doi.org/10.2118/116823-MS.

Alavian, S. A. and Whitson, C. H. 2010. Scale Dependence of Diffusion in Naturally Fractured Reservoirs for CO_2 Injection. Paper presented at the SPE Improved Oil Recovery Symposium, Tulsa, Oklahoma, USA, 24–28 April. SPE-129666-MS. https://doi.org/10.2118/129666-MS.

Ashrafizadeh, S. N. and Ghasrodashti, A. A. 2011. An Investigation on the Applicability of Parachor Model for the Prediction of MMP Using Five Equations of State. *Chem. Eng. Res. Des.* **89** (6): 690–696. https://doi.org/10.1016/j.cherd.2010.10.015.

Ayirala, S. C. and Rao, D. N. 2011. Comparative Evaluation of a New MMP Determination Technique. *J Can Pet Technol* **50** (9/10): 71–81. SPE-99606-PA. https://doi.org/10.2118/99606-PA.

Calsep A/S. 2018. PVTsim Nova, Revision 3. Lyngby, Denmark: Calsep A/S.

Cronin, M., Emami-Meybodi, H., and Johns, R. T. 2019. Diffusion-Dominated Proxy Model for Solvent Injection in Ultratight Oil Reservoirs. *SPE J.* **24** (2): 660–680. SPE-190305-PA. https://doi.org/10.2118/190305-PA.

Dymond, J. H. and Malhotra, R. 1988. The Tait Equation: 100 Years On. *Int J Thermophys* **9** (6): 941–951. https://doi.org/10.1007/BF01133262.

Eghbali, S. and Dehghanpour, H. 2018. An Experimental and Modeling Study of Carbon Dioxide/Bitumen and C_4/Bitumen Phase Behavior at Elevated Temperatures Using Cold Lake Bitumen. *SPE J.* **23** (6): 1991–2014. SPE-187259-PA. https://doi.org/10.2118/187259-PA.

Egwuenu, A. M., Johns, R. T., and Li, Y. 2004. Improved Fluid Characterization for Miscible Gas Floods. *SPE Res Eval & Eng* **11** (4): 655–665. SPE-94034-PA. https://doi.org/10.2118/94034-PA.

Gao, G., Daridon, J.-L., Saint-Guirons, H. et al. 1992. A Simple Correlation to Evaluate Binary Interaction Parameters of the Peng-Robinson Equation of State: Binary Light Hydrocarbon Systems. *Fluid Phase Equilib* **74** (15 July): 85–93. https://doi.org/10.1016/0378-3812(92)85054-C.

Gherabati, S. A., Browning, J., Male, F. et al. 2017. Evaluating Hydrocarbon-in-Place and Recovery Factor in a Hybrid Petroleum System: Case of Bakken and Three Forks in North Dakota. Paper presented at the SPE/AAPG/SEG Unconventional Resources Technology Conference, Austin, Texas, USA, 24–26 July. URTEC-2671498-MS. https://doi.org/10.15530/URTEC-2017-2671498.

Hawthorne, S. B., Miller, D. J., Jin, L. et al. 2016. Rapid and Simple Capillary-Rise/Vanishing Interfacial Tension Method to Determine Crude Oil Minimum Miscibility Pressure: Pure and Mixed CO_2, Methane, and Ethane. *Energy Fuels* **30** (8): 6365–6372. https://doi.org/10.1021/acs.energyfuels.6b01151.

Hoffman, B. T. 2018. Huff-N-Puff Gas Injection Pilot Projects in the Eagle Ford. Paper presented at the SPE Canada Unconventional Resources Conference, Calgary, Canada, 13–14 March. SPE-189816-MS. https://doi.org/10.2118/189816-MS.

Hughes, J. D. 2013. A Reality Check on the Shale Revolution. *Nature* **494:** 307–308. https://doi.org/10.1038/494307a.

Jessen, K. and Orr, F. M. 2008. On Interfacial-Tension Measurements to Estimate Minimum Miscibility Pressures. *SPE Res Eval & Eng* **11** (5): 933–939. SPE-110725-PA. https://doi.org/10.2118/110725-PA.

Jessen, K., Michelsen, M., and Stenby, E. H. 1998. Global Approach for Calculation of Minimum Miscibility Pressure. *Fluid Phase Equilib* **153** (2): 251–263. https://doi.org/10.1016/S0378-3812(98)00414-2.

Jin, L., Hawthorne, S., Sorensen, J. et al. 2017. Utilization of Produced Gas for Improved Oil Recovery and Reduced Emissions from the Bakken Formation. Paper presented at the SPE Health, Safety, Security, Environment, & Social Responsibility Conference–North America, New Orleans, Louisiana, USA, 18–20 April. SPE-184414-MS. https://doi.org/10.2118/184414-MS.

Johns, R. T., Sah, P., and Solano, R. 2002. Effect of Dispersion on Local Displacement Efficiency for Multicomponent Enriched-Gas Floods Above the Minimum Miscibility Enrichment. *SPE Res Eval & Eng* **5** (1): 4–10. SPE-75806-PA. https://doi.org/10.2118/75806-PA.

Katz, D. L. and Firoozabadi, A. 1978. Predicting Phase Behavior of Condensate/Crude Oil Systems Using Methane Interaction Coefficients. *J Pet Technol* **30** (11): 1649–1655. SPE-6721-PA. https://doi.org/10.2118/6721-PA.

Kaul, P. K. 1999. *An Analysis of Phase Behavior and Displacement Characteristics of Multicomponent Mixtures*. PhD dissertation, Stanford University, Stanford, California, USA.

King, G. E. 2014. 60 Years of Multi-Fractured Vertical, Deviated and Horizontal Wells: What Have We Learned? Paper presented at the SPE Annual Technical Conference and Exhibition, Amsterdam, The Netherlands, 27–29 October. SPE-170952-MS. https://doi.org/10.2118/170952-MS.

Kumar, A. 2016. *Characterization of Reservoir Fluids Based on Perturbation from n-Alkanes*. PhD dissertation, University of Alberta, Edmonton, Canada.

Lake, L. W. 1989. *Enhanced Oil Recovery*, first edition. Englewood Cliffs, New Jersey, USA: Prentice Hall.

Lashgari, H. R., Sun, A., Zhang, T. et al. 2019. Evaluation of Carbon Dioxide Storage and Miscible Gas EOR in Shale Oil Reservoirs. *Fuel* **241** (1 April): 1223–1235. https://doi.org/10.1016/j.fuel.2018.11.076.

Li, S. and Luo, P. 2017. Experimental and Simulation Determination of Minimum Miscibility Pressure for a Bakken Tight Oil and Different Injection Gases. *Petroleum* **3** (1): 79–86. https://doi.org/10.1016/j.petlm.2016.11.011.

Liu, S., Sahni, V., Tan, J. et al. 2018. Laboratory Investigation of EOR Techniques for Organic Rich Shales in the Permian Basin. Paper presented at the SPE/AAPG/SEG Unconventional Resources Technology Conference, Houston, Texas, USA, 23–25 July. URTEC-2890074-MS. https://doi.org/10.15530/URTEC-2018-2890074.

Martinsen, S. O., Castiblanco, L. A., Osorio, R. et al. 2010. Advanced Fluid Characterization of Pauto Complex, Colombia. Paper presented at the SPE Annual Technical Conference and Exhibition, Florence, Italy, 19–22 September. SPE-135085-MS. https://doi.org/10.2118/135085-MS.

McGuire, P. R., Okuno, R., Gould, T. L. et al. 2017. Ethane-Based Enhanced Oil Recovery: An Innovative and Profitable Enhanced-Oil-Recovery Opportunity for a Low-Price Environment. *SPE Res Eval & Eng* 20 (1): 42–58. SPE-179565-PA. https://doi.org/10.2118/179565-PA.

Metcalfe, R. S. 1982. Effects of Impurities on Minimum Miscibility Pressures and Minimum Enrichment Levels for CO_2 and Rich-Gas Displacements. *SPE J.* 22 (2): 219–225. SPE-9230-PA. https://doi.org/10.2118/9230-PA.

National Institute of Standards and Technology (NIST). 2018. NIST Chemistry WebBook, NIST Standard Reference Database Number 69, http://webbook.nist.gov/chemistry (accessed April 2019).

Nojabaei, B., Johns, R. T., and Chu, L. 2013. Effect of Capillary Pressure on Phase Behavior in Tight Rocks and Shales. *SPE Res Eval & Eng* 16 (3): 281–289. SPE-159258-PA. https://doi.org/10.2118/159258-PA.

Olorode, O. M., Akkutlu, I. Y., and Efendiev, Y. 2017. Compositional Reservoir-Flow Simulation for Organic-Rich Gas Shale. *SPE J.* 22 (6): 1963–1983. SPE-182667-PA. https://doi.org/10.2118/182667-PA.

Orozco, D., Fragoso, A., Selvan, K. et al. 2020. Eagle Ford Huff 'n' Puff Gas-Injection Pilot: Comparison of Reservoir-Simulation, Material Balance, and Real Performance of the Pilot Well. *SPE Res Eval & Eng* 23 (1): 247–260. SPE-191575-PA. https://doi.org/10.2118/191575-PA.

Orr, F. M. Jr. 2007. *Theory of Gas Injection Processes*, first edition. Holte, Denmark: Tie-Line Publications.

Pedersen, K. S., Christensen, P. L., and Shaikh, J. A. 2015. *Phase Behavior of Petroleum Reservoir Fluids*, second edition. Boca Raton, Florida, USA: CRC Press.

Pedersen, K. S., Thomassen, P., and Fredenslund, A. 1985. Thermodynamics of Petroleum Mixtures Containing Heavy Hydrocarbons. 3. Efficient Flash Calculation Procedures Using the SRK Equation of State. *Ind. Eng. Chem. Process Des. Dev.* 24 (4): 948–954. https://doi.org/10.1021/i200031a009.

Péneloux, A., Rauzy, E., and Fréze, R. 1982. A Consistent Correlation for Redlich-Kwong-Soave Volumes. *Fluid Phase Equilib* 8 (1): 7–23. https://doi.org/10.1016/0378-3812(82)80002-2.

Rao, D. N. 1997. New Technique of Vanishing Interfacial Tension for Miscibility Determination. *Fluid Phase Equilib* 139 (1): 311–324. https://doi.org/10.1016/S0378-3812(97)00180-5.

Robinson, D. B. and Peng, D. Y. 1978. The Characterization of the Heptanes and Heavier Fractions for the GPA Peng-Robinson Programs. Research Report RR-28, Gas Producers Association, Tulsa, Oklahoma, USA.

Teklu, T. W., Alharthy, N., Kazemi, H. et al. 2014. Phase Behavior and Minimum Miscibility Pressure in Nanopores. *SPE Res Eval & Eng* 17 (3): 396–403. SPE-168865-PA. https://doi.org/10.2118/168865-PA.

Wang, Y. and Orr, F. M. Jr. 1997. Analytical Calculation of Minimum Miscibility Pressure. *Fluid Phase Equilib* 139 (1–2): 101–124. https://doi.org/10.1016/S0378-3812(97)00179-9.

Whitson, C. H. and Brulé, M. R. 2000. *Phase Behavior*. Richardson, Texas, USA: Monograph Series, Society of Petroleum Engineers.

Whitson, C. H. 1983. Characterizing Hydrocarbon Plus Fractions. *SPE J.* 23 (4): 683–694. SPE-12233-PA. https://doi.org/10.2118/12233-PA.

Yassin, M. R., Habibi, A., Zolfaghari, A. et al. 2018. An Experimental Study of Nonequilibrium Carbon Dioxide/Oil Interactions. *SPE J.* 23 (5): 1768–1783. SPE-187093-PA. https://doi.org/10.2118/187093-PA.

Yellig, W. F. and Metcalfe, R. S. 1980. Determination and Prediction of CO_2 Minimum Miscibility Pressures (includes associated paper 8876). *J Pet Technol* 32 (1): 160–168. SPE-7477-PA. https://doi.org/10.2118/7477-PA.

Yu, W., Lashgari, H. R., Wu, K. et al. 2015. CO_2 Injection for Enhanced Oil Recovery in Bakken Tight Oil Reservoirs. *Fuel* 159 (1 November): 354–363. https://doi.org/10.1016/j.fuel.2015.06.092.

Zhang, Y., Lashgari, H. R., Di, Y. et al. 2017. Capillary Pressure Effect on Phase Behavior of CO_2/Hydrocarbons in Unconventional Reservoirs. *Fuel* 197 (1 June): 575–582. https://doi.org/10.1016/j.fuel.2017.02.021.

Zhang, K., Nojabaei, B., Ahmadi, K. et al. 2018. Minimum Miscibility Pressure Calculation for Oil Shale and Tight Reservoirs with Large Gas-Oil Capillary Pressure. Paper presented at the SPE/AAPG/SEG Unconventional Resources Technology Conference, Houston, Texas, USA, 23–25 July. URTEC-2901892-MS. https://doi.org/10.15530/URTEC-2018-2901892.

Zick, A. A. 1986. A Combined Condensing/Vaporizing Mechanism in the Displacement of Oil by Enriched Gas. Paper presented at the SPE Annual Technical Conference and Exhibition, New Orleans, Louisiana, USA, 5–8 October. SPE-15493-MS. https://doi.org/10.2118/15493-MS.

Appendix A—Compositional Analysis of Crude Oil and Measured Oil Density at Different Pressures and Temperatures

Please see **Tables A-1 and A-2.**

Carbon Number	T_b (°C)	wt%	Carbon Number	T_b (°C)	wt%
5	36	1.79	50	575	0.64
6	69	3.34	52	584	0.57
7	98	2.99	54	592	0.53
8	126	5.42	56	600	0.47
9	174	12.88	58	608	0.4
10	196	5.71	60	615	0.39
12	216	4.96	62	622	0.35
14	254	9.18	64	629	0.31
16	287	7.07	66	635	0.27
18	316	6.49	68	641	0.26
20	344	5.05	70	647	0.24

Table A-1—Compositional analysis of Montney oil from the simulated distillation method.

Carbon Number	T_b (°C)	wt%	Carbon Number	T_b (°C)	wt%
22	369	4.45	72	653	0.22
24	391	3.63	74	658	0.2
26	412	3.29	76	664	0.17
28	431	2.99	78	670	0.17
30	449	2.56	80	675	0.16
32	466	2	82	681	0.14
34	481	1.88	84	686	0.14
36	496	1.73	86	691	0.12
38	509	1.36	88	695	0.11
40	522	1.34	90	700	0.11
42	534	0.96	92	704	0.1
44	545	1.01	94	708	0.1
46	556	0.74	96	712	0.1
48	566	0.73	98	716	0.09
			100+	…	0.09

Table A-1 (continued)—Compositional analysis of Montney oil from the simulated distillation method.

T (°C)	P (psig)	Density (kg/m³)
30.7	4,000	840.71
30.6	3,004	837.81
30.5	2,002	834.35
30.6	1,501	832.88
30.7	1,000	831.82
30.6	505	829.90
30.6	303	829.26
30.5	100	827.75
30.8	14	827.50
50.2	3,998	832.86
50.1	3,000	829.87
50.0	2,001	826.32
49.9	1,504	824.61
49.9	1,000	823.02
50.0	502	821.24
50.1	300	820.05
50.1	101	818.82
50.1	14	818.50
70.3	4,000	823.87
70.3	3,003	820.06
70.4	2,000	817.00
70.5	1,502	815.61
70.4	1,000	813.95
70.5	500	811.30
70.5	301	810.17
70.6	102	809.04
70.2	14	806.50

Table A-2—Measured density of oil at different pressures and temperatures.

Appendix B—Optimized BIP, Properties of the PCs, and P_{sat} Regression of One- and Two-PC EOS Models

Please see **Tables B-1 through B-6.**

	C_1	C_2	PC
C_1	–	–	–
C_2	0	–	–
PC	0.001	0.002	–

Table B-1—Optimized BIP values for the one-PC EOS model.

Component	z_i	MW	P_c (psi)	T_c (°C)	ω	V_c (cm^3/mol)
C_1	0	16.04	667.17	−82.55	0.008	99.00
C_2	0	30.07	708.37	32.25	0.098	148.00
PC	100	185.54	204.94	353.92	0.616	983.44

Table B-2—Properties of the components in the one-PC EOS model.

C_1/C_2 in Gas/Oil Mixture (mol%)	C_2 in C_1/C_2 Mixture (mol%)	Experimental P_{sat} (psi)	Predictions from EOS Model P_{sat} (psi)
69.8	100	560	536
71.2	70	1,041	1,082
71.0	50.4	1,519	1,478
72.0	30.3	1,948	1,984
AARD (%)			3.20

Table B-3—Experimental and predicted P_{sat} using the one-PC EOS model.

	C_1	PC'$_1$	PC'$_2$
C_1	–	–	–
PC'$_1$	0	–	–
PC'$_2$	0.0025	0	–

Table B-4—Optimized BIP values for the two-PC EOS model.

Component	z_i	MW	P_c (psi)	T_c (°C)	ω	V_c (cm^3/mol)
C_1	0	16.04	667.17	−82.55	0.008	99.00
PC'$_1$	27.70	90.29	434.97	260.48	0.314	382.801
PC'$_2$	72.30	222.02	177.96	404.37	0.693	1077.03

Table B-5—Properties of the components in the two-PC EOS model.

C_1 in C_1/Oil Mixture (mol%)	Experimental P_{sat} (psi)	Predictions from EOS Model P_{sat} (psi)
10.3	320	258
29.5	849	832
49.4	1,640	1,631
70.0	3,305	3,105
AARD (%)		6.97

Table B-6—Experimental and predicted P_{sat} using the two-PC EOS model.

Appendix C—Two-Phase Equilibrium Data Using Four-, Two-, and One-PC EOS Models

Please see **Tables C-1 and C-2** and **Fig. C-1.**

Composition 1	z_i	Vapor	Liquid	K-Values	Composition 5	z_i	Vapor	Liquid	K-Values
C_1	70.000	99.471	57.159	1.74025	C_1	68.300	90.131	51.662	1.74464
PC_1	12.945	0.500	18.368	0.02720	C_2	10.700	9.294	11.772	0.78949
PC_2	8.459	0.026	12.133	0.00211	PC_1	8.945	0.531	15.358	0.03458
PC_3	5.589	0.003	8.023	0.00042	PC_2	6.459	0.036	11.354	0.00320
PC_4	3.007	0.000	4.316	0.00011	PC_3	4.589	0.007	8.082	0.00090
					PC_4	1.007	0.001	1.773	0.00034

Composition 2	z_i	Vapor	Liquid	K-Values	Composition 6	z_i	Vapor	Liquid	K-Values
C_1	77.000	99.471	57.211	1.73866	C_1	78.066	93.950	50.314	1.86728
PC_1	10.000	0.501	18.365	0.02726	C_2	5.982	5.444	6.922	0.78653
PC_2	6.000	0.024	11.263	0.00212	PC_1	7.922	0.567	20.770	0.02732
PC_3	5.000	0.004	9.400	0.00042	PC_2	5.442	0.033	14.894	0.00218
PC_4	2.000	0.000	3.761	0.00011	PC_3	2.582	0.005	7.082	0.00077
					PC_4	0.007	0.000	0.018	0.00040

Composition 3	z_i	Vapor	Liquid	K-Values	Composition 7	z_i	Vapor	Liquid	K-Values
C_1	68.500	99.438	54.833	1.81347	C_1	88.000	97.541	54.193	1.79988
PC_1	15.000	0.532	21.391	0.02486	C_2	2.000	1.875	2.443	0.76756
PC_2	10.000	0.026	14.406	0.00184	PC_1	5.000	0.552	20.761	0.02658
PC_3	5.000	0.003	7.207	0.00045	PC_2	3.000	0.028	13.531	0.00206
PC_4	1.500	0.000	2.162	0.00015	PC_3	1.500	0.004	6.802	0.00052
					PC_4	0.500	0.000	2.270	0.00018

Composition 4	z_i	Vapor	Liquid	K-Values	Composition 8	z_i	Vapor	Liquid	K-Values
C_1	58.698	99.443	56.537	1.75889	C_1	52.000	84.795	50.595	1.67595
PC_1	18.885	0.528	19.859	0.02658	C_2	18.000	14.600	18.146	0.80460
PC_2	12.087	0.026	12.726	0.00204	PC_1	12.000	0.550	12.491	0.04405
PC_3	6.574	0.003	6.922	0.00043	PC_2	9.000	0.045	9.384	0.00480
PC_4	3.756	0.000	3.956	0.00012	PC_3	6.000	0.009	6.257	0.00137
					PC_4	3.000	0.002	3.128	0.00051

Table C-1—Two-phase equilibrium data using the four-PC EOS model with Compositions 1 through 4 for the oil/C_1 systems and Compositions 5 through 8 for the oil/C_1/C_2 systems.

	Composition 9					Composition 13			
	z_i	Vapor	Liquid	K-Values		z_i	Vapor	Liquid	K-Values
C_1	92.000	94.348	91.456	1.03163	C_1	60.500	70.898	60.471	1.17242
PC_1	3.000	2.392	3.141	0.76148	C_2	29.500	26.824	29.507	0.90907
PC_2	5.000	3.260	5.403	0.60331	PC	10.000	2.278	10.022	0.22731
	Composition 10					Composition 14			
	z_i	Vapor	Liquid	K-Values		z_i	Vapor	Liquid	K-Values
C_1	94.000	96.933	89.559	1.08234	C_1	63.000	73.621	60.792	1.21103
PC_1	1.000	0.707	1.444	0.48963	C_2	27.000	24.471	27.526	0.88902
PC_2	5.000	2.360	8.997	0.26229	PC	10.000	1.909	11.682	0.16337
	Composition 11					Composition 15			
	z_i	Vapor	Liquid	K-Values		z_i	Vapor	Liquid	K-Values
C_1	93.000	95.853	90.275	1.06178	C_1	66.000	76.704	61.411	1.24903
PC_1	2.000	1.471	2.505	0.58720	C_2	24.000	21.703	24.985	0.86865
PC_2	5.000	2.676	7.219	0.37069	PC	10.000	1.593	13.604	0.11707
	Composition 12					Composition 16			
	z_i	Vapor	Liquid	K-Values		z_i	Vapor	Liquid	K-Values
C_1	90.500	97.554	89.200	1.09365	C_1	75.000	85.438	64.100	1.33289
PC_1	0.500	0.242	0.548	0.44171	C_2	15.000	13.537	16.528	0.81907
PC_2	9.000	2.205	10.252	0.21504	PC	10.000	1.025	19.372	0.05289

Table C-2—Two-phase equilibrium data using a two-PC EOS model with Compositions 9 through 12 for the oil/C_1 systems and the one-PC EOS model with Compositions 13 through 16 for the oil/C_1/C_2 systems.
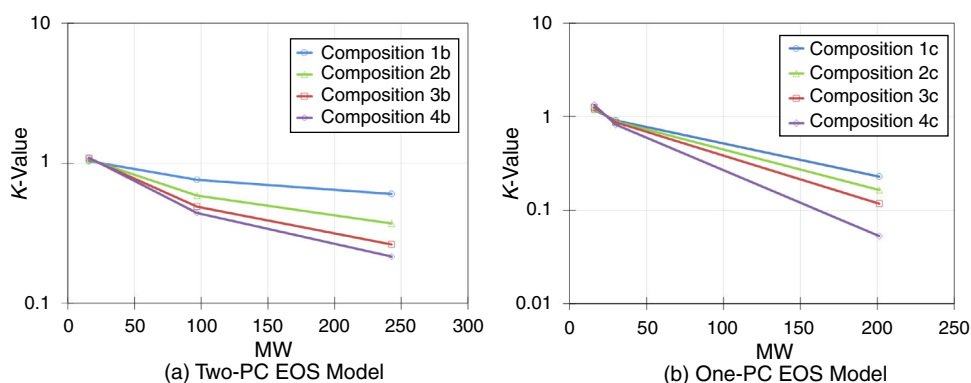

Fig. C-1—Two-phase equilibrium K-values vs. MW of PCs in (a) two-PC EOS model and (b) one-PC EOS model at reservoir pressure and temperature of 2,000 psi and 50°C.